nature catalysis

Article

https://doi.org/10.1038/s41929-023-01023-1

Light-driven synthesis of C_2H_6 from CO_2 and H_2O on a bimetallic AuIr composite supported on InGaN nanowires

Received: 24 August 2021

Accepted: 8 August 2023

Published online: 14 September 2023

Check for updates

Baowen Zhou[1,9,10] ✉, Yongjin Ma[1,2,10], Pengfei Ou[3,4,10], Zhengwei Ye[1,10], Xiao-Yan Li[4], Srinivas Vanka[1], Tao Ma[5], Haiding Sun[6], Ping Wang[1], Peng Zhou[1], Jason K. Cooper[7,8], Yixin Xiao[1], Ishtiaque Ahmed Navid[1], Jun Pan[2], Jun Song[3] ✉ & Zetian Mi[1] ✉

Generation of C_{2+} compounds from sunlight, carbon dioxide and water provides a promising path for carbon neutrality. Central to the construction of a rational artificial photosynthesis integrated device is the requirement for a catalyst to break the bottleneck of C–C coupling. Here, based on operando spectroscopy measurements, theoretical calculations and feedstock experiments, it is discovered that gold, in conjunction with iridium, can catalyse the reduction of CO_2, achieving C–C coupling by insertion of CO_2 into $-CH_3$. Due to a combination of optoelectronic and catalytic properties, the assembly of AuIr with InGaN nanowires on silicon enables the achievement of a C_2H_6 activity of 58.8 mmol g^{-1} h^{-1} with a turnover number of 54,595 over 60 h. A light-to-fuel efficiency of ~0.59% for solar fuel production from CO_2 and H_2O is achieved without any other energy inputs. This work provides a carbon-negative path for producing higher-order carbon compounds.

Recycling of carbon dioxide (CO_2) into clean fuels and chemicals offers an attractive pathway to address the critical issues of energy shortage and climate change[1,2]. Compared with electrocatalysis, thermocatalysis and biocatalysis, which require intensive energy inputs and/or complex set-ups, photocatalysis has emerged as a promising carbon fixation technology because of its simple configuration, low cost and environmental accountability[3–5]. Photocatalytic synthesis of C_{2+} compounds without sacrificial agents is particularly interesting but has remained extremely challenging. Thus far, a broad range of photocatalytic devices have been explored for CO_2 reduction by assembling various semiconductors with suitable catalysts[6,7]. However, state-of-the-art photocatalytic devices predominantly yield C_1 products[8,9] with low activities, of the order of micromoles per gram of catalyst per hour (μmol g^{-1} h^{-1}), and low light-to-fuel (LTF) energy efficiencies of <0.1% (refs. 10–13). Furthermore, sacrificial agents were often required in these studies[14]. These drawbacks could be attributed to the following reasons. First, for most semiconductors, due to their fixed band structures, it is difficult to provide sufficient redox potentials without compromising light absorption[15]. Moreover, there is a lack of an efficient electron-migration channel in the systems, which suffer from

[1]Department of Electrical Engineering and Computer Science, University of Michigan, Ann Arbor, MI, USA. [2]State Key Laboratory for Powder Metallurgy, Central South University, Changsha, P. R. China. [3]Department of Mining and Materials Engineering, McGill University, Montreal, Quebec, Canada. [4]Department of Electrical and Computer Engineering, University of Toronto, Toronto, Ontario, Canada. [5]Michigan Center for Materials Characterization, University of Michigan, Ann Arbor, MI, USA. [6]School of Microelectronics, University of Science and Technology of China, Hefei, P. R. China. [7]Chemical Sciences Division, Lawrence Berkeley National Laboratory, Berkeley, CA, USA. [8]Liquid Sunlight Alliance, Lawrence Berkeley National Laboratory, Berkeley, CA, USA. [9]Present address: Key Laboratory for Power Machinery and Engineering of Ministry of Education, Research Center for Renewable Synthetic Fuel, School of Mechanical Engineering, Shanghai Jiao Tong University, Shanghai, China. [10]These authors contributed equally: Baowen Zhou, Yongjin Ma, Pengfei Ou, Zhengwei Ye. ✉e-mail: zhoubw@sjtu.edu.cn; jun.song2@mcgill.ca; ztmi@umich.edu

a high degree of electron–hole recombination. Most significantly, C–C coupling is a highly endergonic process with sluggish kinetics, and remains a fundamental bottleneck of applied bias-free C_{2+} compound synthesis[16,17]. The exploration of a rationally designed catalyst, coupled with a proper semiconductor light absorber to address the critical issues above, is at the core of breaking the bottleneck of bias-free C_{2+} compound synthesis.

Known catalysts of CO_2 reduction include enzymes[18], molecular catalysts[2,19] and metal/metal oxides[20,21]. Among various materials, copper and its derivatives are widely recognized to be efficient catalysts capable of synthesizing C_{2+} compounds because of their unique properties[22,23]. Through defect engineering, surface reconstruction and oxidation-state tuning, a broad range of C_{2+} compounds, including C_2H_4 and C_2H_5OH, have been produced over copper-based catalysts[24,25]. However, large overpotentials are in principle required to drive the reactions by electrocatalysis. In contrast, photocatalysis presents a simple configuration for generating C_{2+} compounds from CO_2 and H_2O without applied potentials.

III-nitrides have emerged as an important family of semiconductor materials for artificial photosynthesis due to their distinct structural, optical and electronic properties[15]. State-of-the-art molecular beam epitaxy technology has enabled the successful application of III-nitrides to a variety of photocatalytic processes including overall water splitting[26,27] and CO_2 reduction to C_1 products, for example, CO and CH_4[28], thereby demonstrating behaviour distinct from that of conventional semiconductors. III-nitrides thus hold great promise for constructing an artificial photosynthesis integrated device (APID) by coupling a rationally designed catalyst for applied bias-free synthesis of C_{2+} compounds from CO_2 and H_2O.

In this article, gold is coupled with iridium to mediate the reduction of CO_2 to C_{2+} products because of gold's weak interactions with reactants/intermediates, for example, *CO (refs. 29,30). Thus, C–C coupling is achieved by inserting CO_2 into the $-CH_3$ intermediate over AuIr. Benefiting from the distinct properties of one-dimensional (1D) InGaN nanowires (NWs), the assembly of AuIr with 1D InGaN NWs demonstrates the applied bias-free photocatalytic synthesis of C_{2+} compounds from CO_2 and H_2O without sacrificial agents. The conditions for epitaxial growth of 1D InGaN NWs were optimized based on extensive studies of their structural and optoelectronic properties[26,27,31]. In this study, AuIr is integrated with a well-developed semiconductor platform for CO_2 photoreduction to C_{2+} products. A C_2H_6 activity of 58.8 mmol g^{-1} h^{-1} is achieved under concentrated light illumination with an appreciable total selectivity of ~17.6% for CH_4 and C_2H_6. Taking the useful by-products of syngas into consideration, the as-designed device exhibits an LTF efficiency of ~0.59%, with a turnover number of 54,595 for C_2H_6 without obvious performance degradation over 60 h. This work presents an APID for the synthesis of C_{2+} compounds using light, CO_2 and water as the only inputs.

Results

Characterization of AuIr-decorated InGaN NWs

InGaN NWs were epitaxially grown on a 3 inch silicon wafer based on our reported methods[26], followed by photodepositing co-catalysts of gold and/or iridium (Supplementary Figs. 1 and 2). According to previous studies, the conduction band and valence band edges of InGaN NWs shown in Fig. 1a are well positioned with respect to the required redox potentials for CO_2 reduction with water, thermodynamically making it possible to synthesize applied bias-free C_{2+} compounds without sacrificial agents[32]. As characterized by scanning electron microscopy, InGaN NWs vertically aligned on silicon possess an average height of 600–750 nm with lateral sizes varying from 50 to 150 nm at the top region. The loaded co-catalysts do not affect the morphologies of InGaN NWs significantly (Supplementary Fig. 3). The high-angle annular dark-field scanning transmission electron microscopy (HAADF-STEM) and elemental mapping images in Fig. 1b and Supplementary Fig. 4 show that the Au NPs deposited on the surface of InGaN have a high-quality crystal structure. The interplanar lattice spacing of $d = 0.25$ nm is attributed to Au(111), which can be observed at 2θ of 38.2° by X-ray diffraction measurement (Fig. 1d)[33]. A series of binary Au_xIr_{1-x} were further built by coupling with secondary iridium (x presents the molar ratio of Au in the binary AuIr cocatalyst). The introduction of iridium did not affect the crystal structure of Au(111). Furthermore, as characterized by Auger electron spectroscopy, the Au/Ir ratios of this series are estimated to be 0.55/0.45, 0.44/0.56 and 0.26/0.74, respectively. As shown in Fig. 1c, the as-designed Au_xIr_{1-x} binary catalytic system features a bimetallic solid solution. From energy-dispersive spectrometry (EDS) quantification, the Au/Ir ratio on the surface of AuIr is approximately 51/49 while the centre region has a higher proportion of gold, 81% (Supplementary Fig. 5). The total loading amount of gold and iridium in the $Au_{0.44}Ir_{0.56}$/InGaN NWs is evaluated to be 0.012 μmol cm^{-2} by inductively coupled plasma atomic emission spectroscopy (ICP-AES). X-ray photoelectron spectroscopy (XPS) characterization was conducted to study the elemental oxidation states of the artificial photosynthesis integrated devices (Supplementary Figs. 6 and 7). It is observed that the featured peak of Au $4f_{7/2}$ in AuIr@InGaN NWs/Si appears at 83.9 eV, which is positively shifted by +0.6 eV compared with that of Au $4f_{7/2}$ at 83.3 eV in Au NPs@InGa NWs/Si (Fig. 1e). This finding confirms the electronic interaction between gold and iridium in AuIr@InGaN NWs/Si. Such an electronic interaction may increase the likelihood of C–C coupling by influencing the catalytic properties, which will be discussed in the following.

Apart from the catalysts, the semiconductor also plays a vital role in photocatalytic CO_2 reduction by supplying charge carriers with the necessary redox potentials to drive the reactions. As such, the radiative recombination efficiency of charge carriers of InGaN NWs was measured by temperature-dependent photoluminescence (TD-PL) spectroscopy (Fig. 1f). The internal quantum efficiency calculated using the integrated intensity ratio of the PL spectra recorded at 300 K and 10 K (ref. 34), that is, $I_{300\,K}/I_{10\,K}$, is ~5%. The measured internal quantum efficiency signified a low radiative recombination efficiency of the photoexcited electrons and holes in InGaN NWs. The likelihood of the photoexcited charge carriers participating in chemical reactions was enhanced, thus favouring high-efficiency CO_2 reduction. In general, as the distribution of CO_2 reduction products varies as a function of applied potential in electrocatalysis, using tuned PL quantum efficiency could yield tailored CO_2 reduction product distributions for these bias-free photocatalysts. Furthermore, in this study, the NW radius (~25–75 nm) is smaller than the carrier diffusion length in crystalline magnesium-doped p-type GaN (93 ± 7 nm at 295 K)[35]. Therefore, charge carrier extraction to the lateral surfaces of the NWs is extremely efficient, irrespective of whether or not metal particles are present, which is highly favourable for the reaction. This is confirmed by transient reflection spectroscopy measurements of the various samples (Fig. 1g). Moreover, the well-defined 1D morphology of InGaN NWs is highly favourable for absorbing photons by minimizing light reflection (Supplementary Fig. 8), which has been confirmed in our previous works[36,37]. Together, AuIr@GaN NWs/Si hold great promise for highly efficient photocatalytic CO_2 reduction due to their outstanding optical, electronic and catalytic properties.

Photocatalytic performance

The reactions were carried out in a home-made glass chamber in CO_2 aqueous solution under concentrated light illumination of 3.5 W cm^{-2} without any applied bias or sacrificial agents (Supplementary Fig. 9). Without catalysts, InGaN NWs show little hydrogen evolution activity and no carbon products. With the decoration of various amounts of gold, InGaN NWs/Si exhibit considerable CO_2 reduction activity (Fig. 2a,b). As expected, C_1 compounds are preferably produced by gold, and CO is the major carbon product[38,39]. The activity and selectivity largely depend on the properties of the Au NPs (Supplementary Fig. 10)[40]. The formation rate of CO increases with gold loading and

https://doi.org/10.1038/s41929-023-01023-1

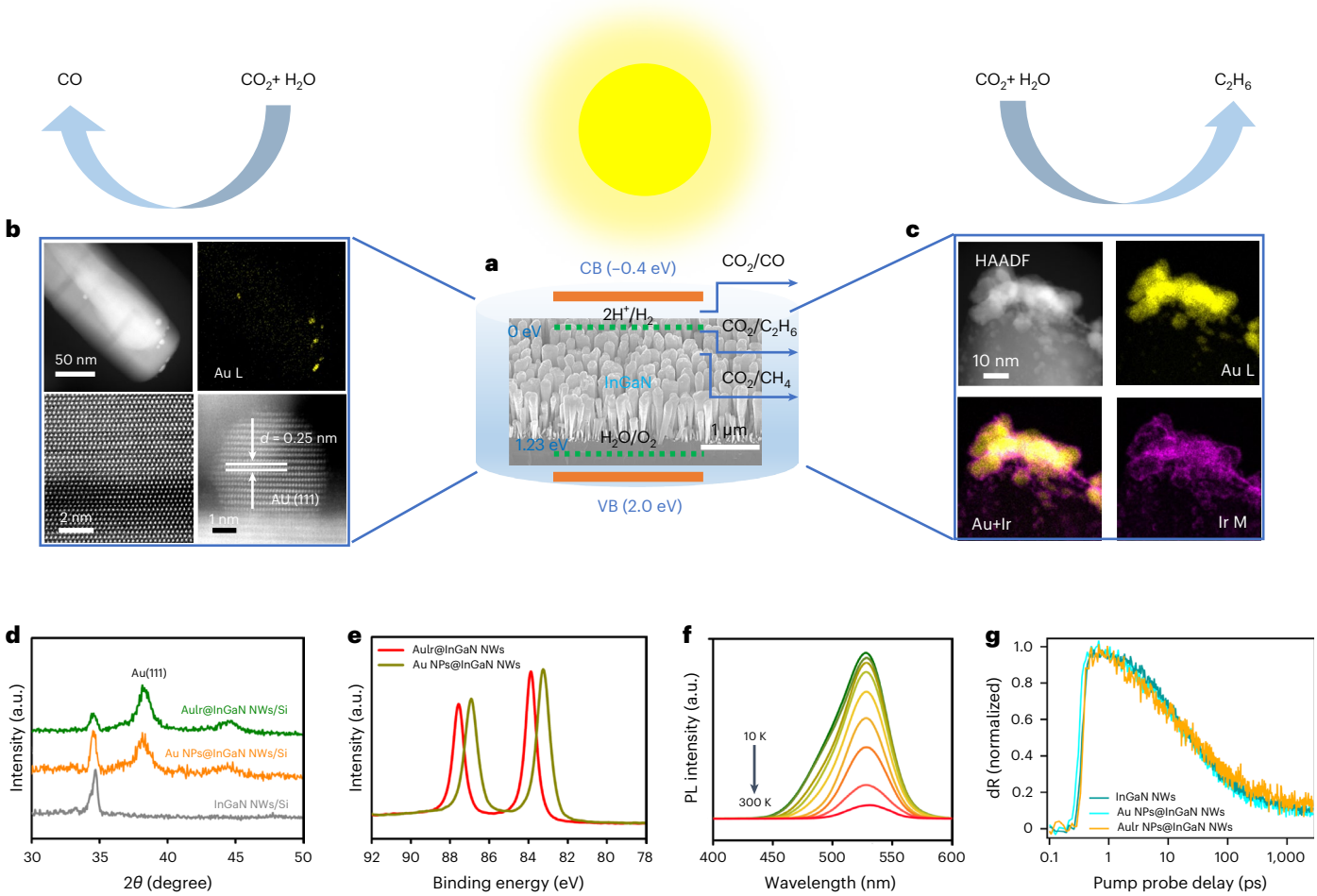

Fig. 1 | Characterization of AuIr-decorated InGaN NWs. a, A 45° tilted SEM image and energy band structure of InGaN NWs/Si. CB, conduction band; VB, valence band. **b**,**c**, HAADF-STEM and elemental mapping images of Au NPs@InGaN NWs (**b**) and AuIr@InGa NWs/Si (**c**). **d**, X-ray diffraction spectra of InGaN NWs/Si, Au NPs@InGaN NWs/Si and AuIr@InGaN NWs/Si. **e**, High-resolution XPS spectra of Au 4*f*. **f**, Temperature-dependent photoluminescence spectroscopy of InGaN NWs/Si. **g**, Transient reflection spectroscopy of InGaN NWs and Au NP- and AuIr-decorated InGaN NWs/Si.

reaches a peak value of 38.4 mmol g^{-1} h^{-1} with a selectivity of 9.6% at an average Au NP size of 6.0 nm. In this case, the hydrogen evolution reaction (HER) is much more favoured compared with CO_2 reduction and the selectivity of H_2 is as high as 85.7%, further suggesting the challenge of selective conversion of CO_2. Reduced performance of CO (24.6 mmol g^{-1} h^{-1}) is observed at a higher gold loading, probably originating from the decreased catalytic activity as the size of the Au NPs further increases up to 10.4 nm (ref. 41). To gain an overall view of the reaction, the evolution of CO_2 reduction products over the optimized Au_2@InGaN NWs/Si was tested as a function of the illumination time. As shown in Fig. 2c, CO is the dominant product, accompanied by CH_4 evolved as the by-product. Over the time range examined, C_{2+} compounds are not detected over pure gold, confirming that gold is not capable of catalysing C–C coupling toward C_{2+} compounds. However, the performance of AuIr@InGaN NWs/Si is very different from that of Au NPs@InGaN NWs (Fig. 2d,e). The overall activity of various products is significantly improved by the addition of iridium. More importantly, AuIr@InGaN NWs demonstrate C_2H_6 synthesis activity. In terms of the activity of CH_4 and C_2H_6, AuIr@InGaN NWs/Si compare favourably with previously reported photocatalytic devices. As shown in Supplementary Table 1, most of the previously reported photocatalytic devices only showed low CH_4 activity on the order of μmol g^{-1} h^{-1} and were almost inactive for C_{2+} compound synthesis. In stark contrast, a C_2H_6 evolution rate of 58.8 mmol g^{-1} h^{-1} is achieved by $Au_{0.44}Ir_{0.56}$@InGaN NWs/Si with a selectivity of 5.6%. Meanwhile, the formation rate of CH_4 is as high as 125.4 mmol g^{-1} h^{-1}, which is several orders of magnitude higher than that of state-of-the-art catalytic systems (Supplementary Table 1). The total selectivity of hydrocarbons, including CH_4 and C_2H_6, reaches 17.6%. It is worth emphasizing that a mixture of CO and H_2, an important chemical feedstock named syngas, is formed as a useful by-product with an appreciable activity of 863.4 mmol g^{-1} h^{-1} (H_2, 735.6 mmol g^{-1} h^{-1}; CO, 127.8 mmol g^{-1} h^{-1}) and a high selectivity of 82.4%. Taking all the photocatalysis products into consideration, an LTF efficiency of 0.59% is achieved with $Au_{0.44}Ir_{0.56}$@InGaN NWs/Si (Fig. 2f), which is 3.5 times higher than that of Au NPs@InGaN NWs/Si (0.17%). Moreover, Ir@InGaN NWs are also active for C_2H_6 formation, albeit with much lower activity (3.3 mmol g^{-1} h^{-1}) and lower selectivity (0.31%) than that of AuIr@InGaN NWs. These findings validate that iridium is critical for C–C bond formation. As further demonstrated by the control experiments in Supplementary Table 2, the reaction did not occur if AuIr was directly deposited on silicon (characterized by SEM in Supplementary Fig. 11) because silicon was not able to produce energetic charge carriers for CO_2 reduction due to its narrow bandgap. Hence, both AuIr and InGaN NWs are indispensable for the conversion of CO_2 to C_2H_6. The optimized precursor ratio was applied in the following experiments. The influence of light intensity on the reaction was studied (Supplementary Fig. 12). Under relatively weak light intensity, varying from 0.1 to 0.5 W cm^{-2}, the photocatalytic

https://doi.org/10.1038/s41929-023-01023-1

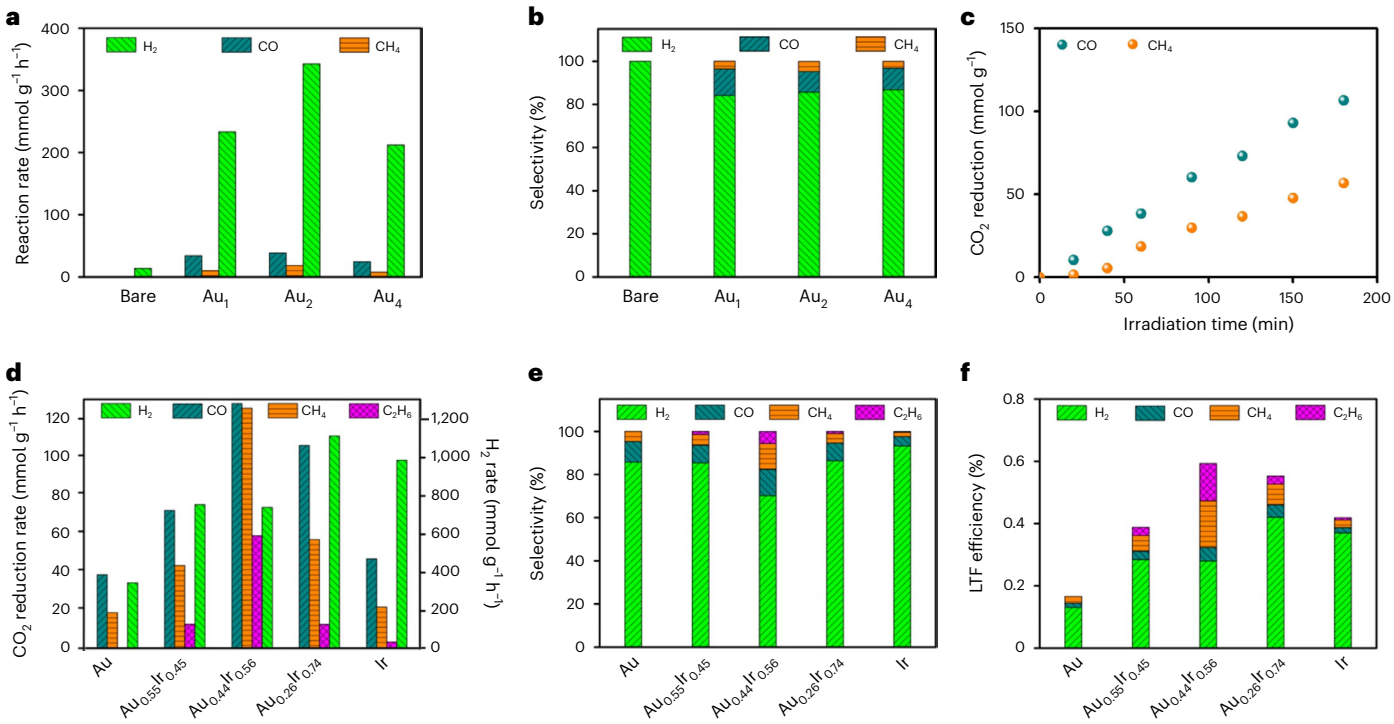

Fig. 2 | Photocatalytic activity of AuIr-decorated InGaN NWs. a,**b**, Evolution rate (**a**) and selectivity (**b**) of different products from photocatalytic CO_2 reduction over Au NPs@InGaN NWs/Si decorated with various amounts of gold. **c**, Time course of CO and CH_4 evolved from the CO_2 reduction reaction over Au_2@InGaN NWs/Si. **d**–**f**, Evolution rate (**d**), selectivity (**e**) and LTF efficiencies (**f**) of various products from photocatalytic CO_2 reduction over AuIr@InGaN NWs/Si with various Au/Ir ratios. Experimental conditions: 30 ml distilled water, CO_2, 300 W xenon lamp, 3.5 W cm^{-2}. (The data have a 5–10% error bar during sampling).

activity was low. This could be attributed to the insufficient number of photogenerated electron–hole pairs, which is consistent with previous studies[26]. In contrast, under high light intensity, above 1.5 W cm^{-2}, the efficiency of CO_2 reduction was sharply increased by the continuously increasing light intensity. Under concentrated light illumination of 3.5 W cm^{-2}, InGaN NWs are photoexcited to produce abundant electrons and holes. The photogenerated electrons will then migrate to the deposited AuIr for CO_2 reduction and hydrogen evolution while the holes will be consumed by water oxidation (Supplementary Fig. 13). Here, the photothermally assisted effect of concentrated light illumination on the reaction was also investigated. As measured by a thermocouple, increasing light intensity led to an enhanced heating rate of the reaction system because of the photothermal effect (Supplementary Fig. 14). Moreover, it was found that under three concentrated light illuminations of 1.5, 2.5 and 3.5 W cm^{-2}, activity was increased as the waterbath temperature was raised from 20 °C to 50 °C by an external temperature-control system (Supplementary Fig. 15). Further increasing the temperature, however, did not show an obvious enhancement in performance. The lowered CO_2 solubility in water at higher temperatures contributed to this process (Supplementary Fig. 16). Meanwhile, under ultraviolet light illumination, the architecture exhibited only moderate photocatalytic CO_2 reduction activity (Supplementary Fig. 17). In stark contrast, the architecture was hardly active for photocatalytic CO_2 reduction illuminated by infrared light because the infrared light cannot excite InGaN NWs to offer photogenerated charge carriers (Supplementary Table 2). These results suggest that the reaction proceeds via thermally assisted photocatalysis, and the photogenerated charge carriers play a prominent role in the superior performance. It is also noted that in the absence of CO_2, no carbon-derived products except for hydrogen were detected from photoreduction by the same catalyst of $Au_{0.44}Ir_{0.56}$@InGaN NWs/Si under vacuum without varying other experimental conditions, for example, light intensity of 3.5 W cm^{-2}. To further verify the source of the C_{2+} photoreduction products, an isotopic test was conducted by feeding ^{13}C-labelled CO_2 and the results are shown in Supplementary Fig. 18. It is observed that the typical features of $^{13}C_2H_6$ were detected by gas chromatography–mass spectroscopy (Shimadzu QP-2010 GCMS), providing solid evidence that the C_{2+} products originated from CO_2 reduction. The oxidation reaction, which is critical for the entire artificial photosynthesis, was further studied. Gas chromatography reveals that, although not stoichiometric, oxygen was produced from the oxidation half-reaction, along with formation of H_2, CO, CH_4 and C_2H_6 from the reduction half-reaction side (Supplementary Fig. 19). Meanwhile, the formation of H_2O_2 from water oxidation was also determined by using aqueous potassium permanganate solution (Supplementary Fig. 20). Furthermore, a control experiment showed that under high-intensity ultraviolet light, O_2 could be consumed, probably by forming other oxygen species, for example, singlet oxygen, although this is hard to quantify (Supplementary Fig. 21). Taken together, the above results present an artificial photosynthesis process of photocatalytic CO_2 reduction toward various products over AuIr@InGaN NWs/Si, with concurrent water oxidation to H_2O_2, O_2 and other oxygen species.

To further evaluate the intrinsic activity of the optimized $Au_{0.44}Ir_{0.56}$@InGaN NWs/Si, the turnover frequency (TOF), turnover number (TON), evolution rates and yields of various products from CO_2 reduction were measured. Over 60 h of illumination, the TOF of C_2H_6 did not vary very much (average, 910 h^{-1}) (Fig. 3a), and the TON reached 54,595 (Supplementary Fig. 22). A total C_2H_6 yield of 3,275.7 mmol g^{-1} was achieved with an average rate of 54.6 mmol g^{-1} h^{-1} (Fig. 3d and Supplementary Fig. 23). Both CH_4 and CO exhibited a similar tendency to form C_2H_6. The TOF of CH_4 shown in Fig. 3b could be sustained at a high value of 2,681 h^{-1} whereas the TOF of CO exhibited relatively wide variations (Fig. 3c). Meanwhile, CH_4 could be produced at an average rate of 160.9 mmol g^{-1} h^{-1} with a total yield

https://doi.org/10.1038/s41929-023-01023-1

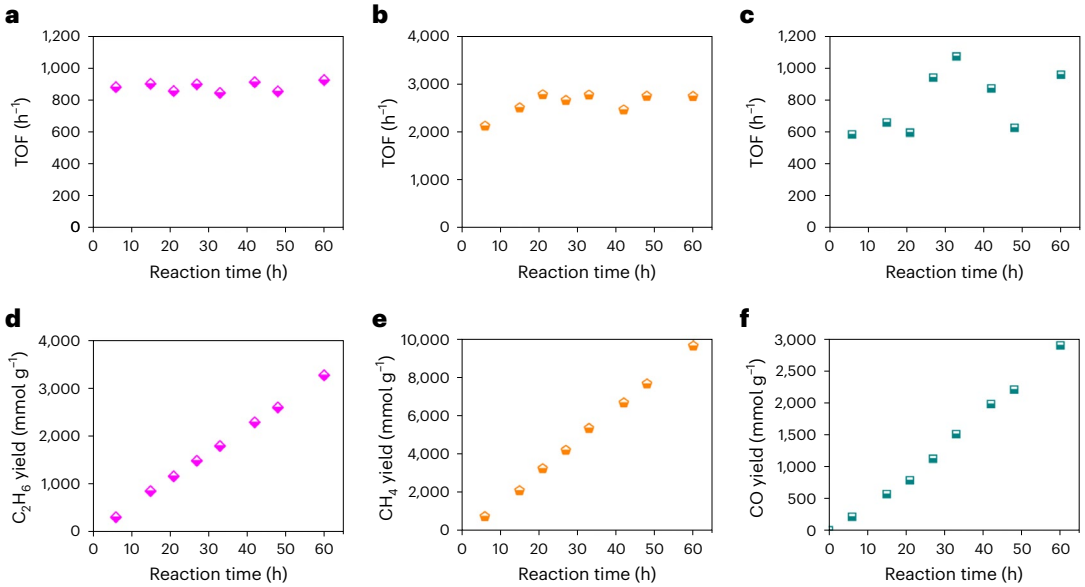

Fig. 3 | Stability testing of various photocatalytic CO_2 reduction products. **a**–**c**, TOF of C_2H_6 (**a**), CH_4 (**b**) and CO (**c**) from photocatalytic CO_2 reduction over $Au_{0.44}Ir_{0.56}$@InGaN NWs/Si in water. **d**–**f**, Yield of C_2H_6 (**d**), CH_4 (**e**) and CO (**f**) from photocatalytic CO_2 reduction over $Au_{0.44}Ir_{0.56}$@InGaN NWs/Si in water. Experimental conditions: 30 ml distilled water, CO_2, 300 W xenon lamp, 3.5 W cm^{-2}.

of 9,653.1 mmol g^{-1}. Such high performance is attributed to the synergism of high optical absorption, high charge carrier extraction efficiency, and unique catalytic properties. The morphology remains nearly intact after long-term testing (Supplementary Fig. 24). Furthermore, as measured by ICP-AES, no elemental indium and gallium was observed in the post-reaction media, indicating the high stability of the epitaxial InGaN NWs. As suggested by our previous studies[42,43], the nitrogen-rich surface, together with the ionic bonds of III-nitrides, can function as a protection layer against photocorrosion. However, harsh operating conditions, for example, high light intensity, led to the deposited gold and iridium being lost from the NWs after 60 h of operation, which was validated by ICP-AES measurements. This causes the degradation of the photocatalytic activity.

Mechanism investigation

To gain more insight into the outstanding performance of the catalyst, the TOFs of C_2H_6 from various feedstocks, for example, CO_2, CO, HCOOH, CH_3COOH and $CH_4 + CO_2$, were estimated in distilled water over $Au_{0.45}Ir_{0.55}$@InGaN NWs/Si under identical experimental conditions (Fig. 4a). Because CO dimerization has been widely recognized as the critical step of C–C coupling during CO_2 reduction[44,45], CO was used as the first feedstock. Surprisingly, it is found that $Au_{0.44}Ir_{0.56}$@InGaN NWs/Si are not active for catalysing C_2H_6 synthesis in the presence of CO, and the same behaviour was seen with HCOOH. In stark contrast, the TOF of C_2H_6 was significantly improved by a factor of 35.5 when using CH_3COOH as the feedstock, and approached 29,543 h^{-1}. Meanwhile, C_2H_6 demonstrated a nearly 20-fold enhancement in TOF when CH_4 was mixed with the CO_2. These results exclude the possibility that C_2H_6 is formed from C–C coupling via the dimerization of CO. To uncover the reaction mechanism, in situ diffuse reflectance infrared Fourier-transform (DRIFT) spectroscopy was further employed to investigate CO_2 reduction at the molecular level. It is found that all the featured signals over $Au_{0.44}Ir_{0.56}$@InGaN NWs/Si are strengthened with irradiation time over a period of 0–20 min (Fig. 4b), whereas Au@InGaN NWs/Si did not exhibit peaks from CO_2 reduction because of the weak interaction between Au NPs and the reactants/intermediates (Supplementary Fig. 25). In particular, the peaks at 1,750 cm^{-1} are associated with the stretching model of the adsorbed C=O species ($\nu_{C=O}$)[44]. Meanwhile, the double peaks in the range of 2,700–3,000 cm^{-1} are related to the vibrational absorption of C–H (ν_{C-H}), and the peaks at 1,450 and 1,370 cm^{-1} originate from the deformation of the vibration model of δ_{C-H}. Based on the above observations, it is suggested that the key intermediate of C_2H_6 contains $-CH_x$ and C=O groups, and the insertion of CO_2 into $-CH_3$ is probably the key step of C–C coupling, which was previously observed during CH_4 reforming with CO_2 over a zinc-doped cerium catalyst[46].

To provide further theoretical insights into the mechanism of C_2H_6 formation, density functional theory (DFT) calculations were conducted over four different surface compositions (Au_xIr_y) on the (111) facet, that is, $Au_{4-x}Ir_x$ ($x = 0, 1, 2, 3$) alloys. We first estimated the reaction energy (ΔG) of multiple elementary steps and their bifurcate routes before C–C coupling occurs (Supplementary Fig. 26). Au_2Ir_2 exhibits the minimum value for the potential-determining step, which is the *CH protonation to $*CH_2$, among the screened Au–Ir compositions. We then focus on Au_2Ir_2 and further performed DFT calculations on the reaction mechanism of direct C–C coupling by considering $*CH + *CH \rightarrow *C_2H_2$, $*CH_2 + *CH_2 \rightarrow *C_2H_4$, $*CH_3 + *CH_3 \rightarrow C_2H_6(g)$ and CO_2 insertion into $*CH_3$ to $*CH_3COO$. We find that the insertion of CO_2 into $*CH_3$ toward $*CH_3COO$ exhibits the lowest reaction energy and energy barrier simultaneously (Fig. 4c and Supplementary Figs. 27 and 28), and therefore propose this is the possible mechanism of C–C coupling for C_2H_6 synthesis. These theoretical observations are consistent with the operando spectroscopy measurements and feedstock control experiments. The TOF of C_2H_6 using $CH_2OHCOOH$ as the feedstock is about 89.2 h^{-1}, which is 331 times lower than that using CH_3COOH as the intermediate. In addition, we summarize the free energy diagram of the reaction pathway before C–C coupling on the Au_2Ir_2(111) facet in Fig. 4d, that is, CO_2 first adsorbs and is hydrogenated into COH (other than *CHO), then *COH will be further hydrogenated into *C, *CH, $*CH_2$ and $*CH_3$, and finally, another $*CO_2$ inserts the formed $*CH_3$ intermediate to generate the $*CH_3COO$ intermediate. We note that the iridium sites in Au–Ir alloys increase CO_2 reduction activity by lowering the reaction energy of key elementary steps (for example, CO_2 to *COOH on pure gold and *CO to *CHO on Au_3Ir_1 alloy) and steer the selectivity from the dominant HER to C–C coupling with the optimal

https://doi.org/10.1038/s41929-023-01023-1

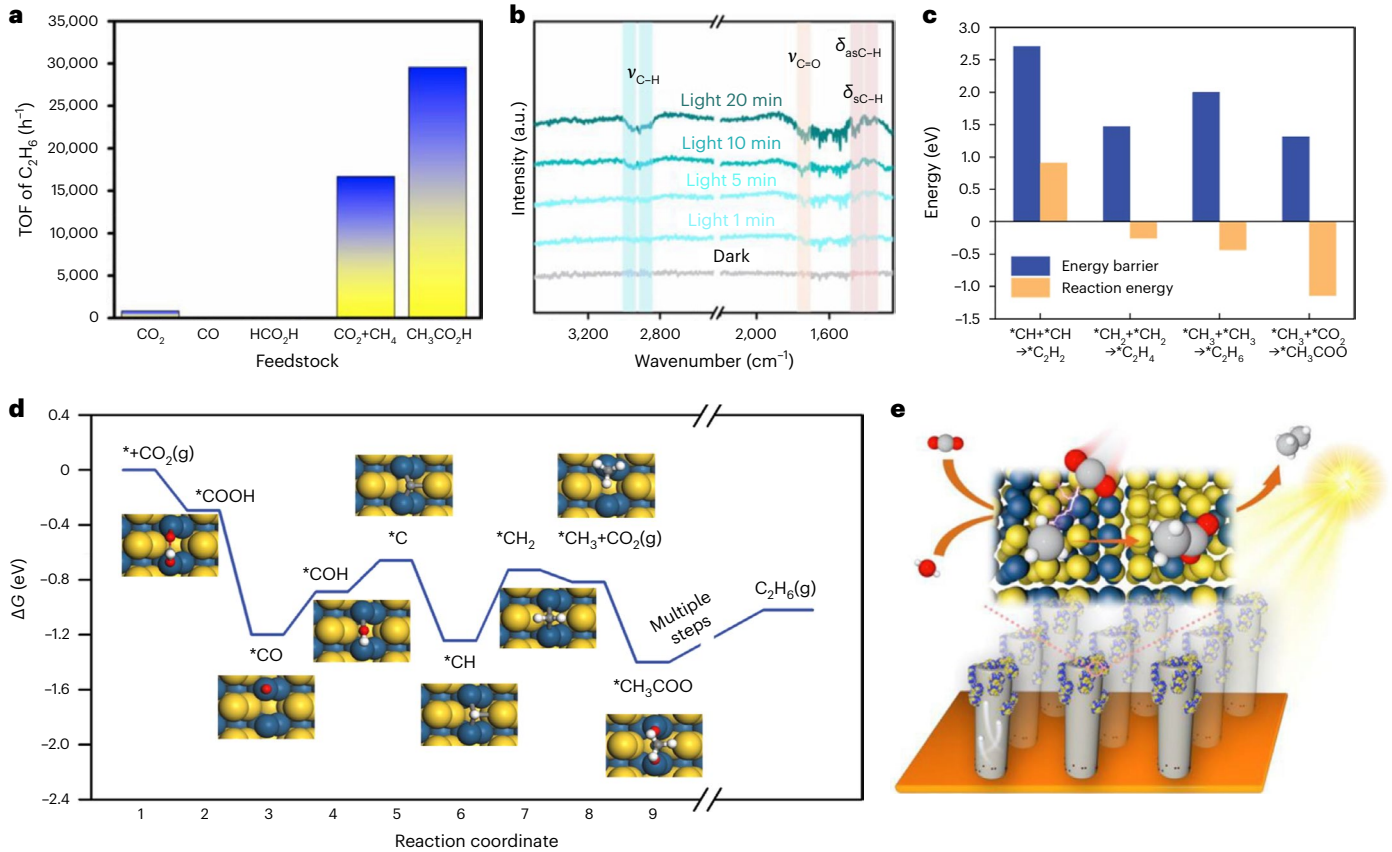

Fig. 4 | Mechanism investigation. a, The TOF of C_2H_6 for various feedstocks in water over $Au_{0.44}Ir_{0.56}$@InGaN NWs/Si. Experimental conditions: 30 ml distilled water, 300 W xenon lamp, 3.5 W cm^{-2}. **b**, DRIFT spectra recorded from photocatalytic CO_2 reduction over $Au_{0.44}Ir_{0.56}$@InGaN NWs/Si. **c**, Calculated reaction energy (orange column) and energy barrier (blue column) of different C–C coupling mechanisms on the Au_2Ir_2(111) facet, including *CH + *CH → *C_2H_2, *CH_2 + *CH_2 → *C_2H_4, *CH_3 + *CH_3 → C_2H_6(g), and CO_2 insertion into *CH_3, that is, *CH_3 + CO_2(g) → *CH_3COO. **d**, Free energy diagram of the reaction pathway before C–C coupling on the Au_2Ir_2(111) facet. Yellow, blue, red, grey and white spheres represent gold, iridium, oxygen, carbon and hydrogen atoms, respectively. **e**, Schematic of light-driven C–C coupling from CO_2 and H_2O over $Au_{0.44}Ir_{0.56}$@InGaN NWs/Si.

value achieved with an Au:Ir ratio of ~1. The synergy between gold and iridium for enhancing photocatalytic CO_2 reduction is decreased if a large portion of iridium is added into gold (for example, $Au_{0.24}Ir_{0.76}$). Based on the above feedstock experiments, operando spectroscopy measurements and theoretical calculations, it is proposed that gold could be mediated by iridium to achieve C–C coupling by insertion of CO_2 into *CH_3, thus facilitating C_2H_6 synthesis from CO_2 and H_2O over AuIr@InGa NWs/Si (Fig. 4e).

Conclusions

The key discovery of this work is the unique mediation of gold by iridium to break the bottleneck of C–C coupling during light-mediated CO_2 reduction. The assembly of AuIr with InGaN NWs illustrates a method for C_2 alkane synthesis from CO_2 and H_2O without using any external bias or any sacrificial agents, due to the distinct catalytic properties of AuIr together with the high optical absorption and high charge charrier efficiency of InGaN NWs. An activity of 58.8 mmol g^{-1} h^{-1} and an appreciable TON of 54,595 over 60 h is achieved for C_2H_6, accompanied by the generation of CH_4 and syngas as useful by-products. The LTF efficiency is approximately 0.59%. Operando spectroscopy measurements, together with theoretical calculation and feedstock experiments, reveal that the insertion of CO_2 into $-CH_3$ is the most likely step of C–C bond formation over AuIr@InGaN NWs/Si. This work has therefore introduced an effective APID for direct production of C_{2+} hydrocarbon synthesis using light, CO_2 and water as the only inputs.

Methods

Epitaxial growth of InGaN NWs

InGaN NWs were grown using a Veeco Gen II MBE system equipped with a radiofrequency plasma-assisted nitrogen source. A 3 inch silicon wafer was used as the substrate. Prior to loading into the MBE chamber, the silicon wafer was washed with acetone and methanol to eliminate organic contaminants, followed by rinsing with 10% hydrofluoric acid to remove silicon oxides. The growth conditions for these NWs were a gallium beam equivalent pressure of 5×10^{-8} torr, an indium beam equivalent pressure of 4×10^{-8} torr and a forward plasma power of 350 W. The nitrogen flow rate is set to be 1.0 standard cubic centimetres per minute (sccm), ensuring a nitrogen-rich atmosphere to promote the formation of a N-terminated lateral surface (m-plane) of the NWs. In addition, the use of gallium seeding layer to promote the formation of a gallium polar basal plane is also critical for N-termination. The substrate temperature for the growth is ~700 °C. Typically, a bottom GaN layer was first in situ grown to serve as the template for the InGaN NWs. Subsequently, five segments of InGaN were deposited on GaN NWs with a growth duration of 40 min. A GaN spacing layer was grown with 10 min between InGaN segments. Magnesium doping was employed throughout the structure to tune the surface band bending of the NWs.

Assembly of Au NPs@InGaN NWs/Si

InGaN NWs/Si were immersed into 1 mol l^{-1} HCl for 10 min to remove surface impurities. The pretreated InGaN NWs/Si (geometry surface

area, ~0.2 cm^2) were rinsed with distilled water and then placed into a 400 ml glass chamber equipped with a top quartz window. Then, 60 ml CH_3OH/H_2O mixture (10/50) was poured into the chamber, followed by the addition of the desired volume of gold precursor (H_2AuCl_4, 0.2 mol l^{-1}). The chamber was then evacuated for ~20 min to remove any air in the system. A 300 W xenon lamp (Cermax, PE300BUV) was utilized as the light source for gold photodeposition with an illumination time of 30 min. The assembled Au NPs@InGaN NWs/Si were rinsed with distilled water to remove carbon residuals.

Assembly of AuIr@InGaN NWs/Si

Using Au@InGaN NWs as the parental template, iridium was further deposited onto Au@p-InGaN NWs/Si using the aforementioned procedure in various concentrations of iridium chloride aqueous solution. Finally, the as-synthesized AuIr@InGaN NWs/Si were rinsed with distilled water to remove residual carbon and dried by nitrogen again. AuIr/Si was prepared for comparison by the same procedure in the absence of InGaN NWs.

Characterization of the devices

The STEM work was conducted using a JEOL 3100R05 double-corrected S/TEM operated at 300 kV. Energy-dispersive X-ray spectroscopy elemental mapping was carried out on a Thermo Fisher Scientific Talos F200X S/TEM equipped with a Super-X detector. SEM characterization was performed on a FEI Helios 650 NanoLab at the Materials Characterizations Center, University of Michigan. The loading density of AuIr was evaluated by ICP-AES (Perkin-Elmer Nexion 2000 Series). The samples were dissolved in aqua regia (HNO_3:HCl, 1:3) for 2 h prior to testing. The optical property measurements were analysed by ultraviolet–visible–near-infrared spectroscopy (Thermo Scientific Evolution 600). The X-ray photoelectron spectroscopies of artificial photosynthesis devices were collected using a Kratos Axis Ultra XPS with a monochromatic Al source at ~10 mA and ~15 V. The binding energy of Ga 3*d* was used for the internal calibration. The room temperature photoluminescence spectroscopy measurements were conducted using either a 325 nm He–Cd laser or a 405 nm laser as the excitation source. The X-ray diffraction profile data were collected on Rigaku Ultima IV in grazing incident mode with an incident angle of 0.5°. The Cu Kα line was utilized for the irradiation, and the diffraction/scattering signals were recorded using a scintillation count detector. AES data were collected on a PHI 680 Auger nanoprobe equipped with a field emission electron gun and a cylindrical mirror energy analyser. Transient reflection spectroscopy was recorded at an excitation wavelength of 350 nm with an excitation power of 40 nJ per pulse and probe wavelength of 650 nm.

Photocatalytic reactions

Unless specifically noted, photocatalytic reactions of CO_2 with H_2O were performed in a home-made sealed glass chamber (diameter, 5 cm; volume, 400 ml) equipped with a top quartz lip under 300 W xenon lamp illumination without filter. Prior to illumination, 30 ml distilled water was purged with high-purity CO_2 (PurityPlus, 99.8%) for 30 min and then poured into the chamber. Subsequently, the chamber was completely evacuated to remove air from the system. The evacuated chamber was then filled with high-purity CO_2 (99.9%) to 2 atm, followed by an illumination step with a light intensity of 3.5 W cm^{-2}. By contrast, to clarify the origin of the carbonaceous products, a control experiment was conducted by illuminating the vacuum distilled water (30 ml) in the absence of CO_2 with a 300 W xenon lamp at a light intensity of 3.5 W cm^{-2} without changing the other conditions. The gaseous products were qualitatively and quantitatively analysed by gas chromatography with a flame ionization detector (GC 2014, Shimadzu) and a thermal conductivity detector (GC 2010, Shimadzu). The liquid reaction mixtures were analysed by NMR spectroscopy (500M, Bruker) using 1,3,5-trioxane as an internal standard. During the long-term operation of 60 h the chamber was evacuated and then purged with CO_2 again before the next run at intervals of 6, 9 or 12 h. The performance was evaluated on the basis of accumulated data.

Calculation of activity and selectivity of H_2, CO, CH_4 and C_2H_6, and LTF efficiency

$$\text{Activity} = \frac{\text{Yield}}{(\text{Surface} \times W \times T)} \quad (1)$$

$$\text{Selectivity of ethane} = \frac{\text{Rate}_{\text{ethane}}}{(\text{Rate}_{\text{H2}} + \text{Rate}_{\text{CO}} + \text{Rate}_{\text{methane}} + \text{Rate}_{\text{ethane}})} \quad (2)$$

$$\text{TON} = \frac{\text{Yield}}{(\text{Surface} \times \text{Loading Density})} \quad (3)$$

$$\text{TOF} = \frac{\text{Yield}}{(\text{Surface} \times \text{Loading Density} \times T)} \quad (4)$$

$$\text{LTF} = \frac{\Delta H_{\text{H2}} \times \text{Yield}_{\text{H2}} + \Delta H_{\text{CO}} \times \text{Yield}_{\text{CO}} + \Delta H_{\text{methane}} \times \text{Yield}_{\text{methane}} + \Delta H_{\text{ethane}} \times \text{Yield}_{\text{ethane}}}{(\text{Light Intensity} \times \text{Surface} \times T)} \quad (5)$$

where Surface is the geometric surface of the sample (~0.3 cm^2); W is the total weight of the epitaxial of InGaN NWs, which is estimated to be ~0.17 mg/cm^2, without considering the trace amount of the co-catalysts; Rate is the evolution rate of each product; Yield is the amount of each product produced; and T is the illumination time. The Loading Density of the AuIr co-catalyst is evaluated to be 0.012 μmol cm^{-2} by ICP-AES. ΔH represents the standard molar enthalpy of combustion of specific products.

DRIFT spectroscopy characterization

In situ DRIFT spectroscopy analysis was conducted using a Bruker IFS 66v Fourier-transform spectrometer with a Harrick diffuse reflectance accessory at the Infrared Spectroscopy and Microspectroscopy Endstation (BL01B), National Synchrotron Radiation Laboratory (NSRL), Hefei. Each spectrum was recorded by averaging 128 scans at a resolution of 2 cm^{-1}. The NW arrays are placed horizontally in the sample chamber. Prior to exposure to CO_2 (99.9999%) atmosphere and illumination, a spectrum is collected as background. During the in situ characterization, water-vapour-saturated CO_2 is introduced into the sample chamber, and a xenon lamp (PLS-SXE300, Perfect Light) is used as a full-spectrum light source. Spectra are recorded in the dark and under illumination for a specific time.

Transient reflection spectroscopy

Optical pump–optical probe transient absorption spectroscopy was performed using a 100 fs, 1 kHz, titanium:sapphire regenerative amplifier (Coherent Libra). A portion of the laser output was coupled to an optical parametric amplifier (Coherent OPerA Solo) to generating a 350 nm pump beam with a diameter of 0.3 mm and a pulse energy of 0.8 μJ at the sample. The supercontinuum probe in the visible region was generated using a sapphire crystal. The incident angle of the probe beam was approximately 8° with respect to the sample surface normal. An ultrafast transient absorption system, equipped with two sets of fibre-coupled grating spectrometers plus silicon CMOS detector arrays, was used for data collection.

DFT calculations

DFT calculations were performed with the Perdew–Burke–Ernzerhof exchange-correlation functional[47] as implemented in Vienna Ab initio Simulation Package[48,49] A plane-wave cut-off energy of 450 eV with a 3 × 3 × 1 Γ-centred *k*-point sampling generated by the Monkhorst–Pack scheme[50] was used for all calculations. A threshold of 10^{-5} eV was used for the convergence of the electronic structure. Optimized structures

were obtained by minimizing the forces on each ion until they fell below 0.01 eV Å^{-1}. The long-range dispersion correction was considered by the zero damping DFT-D3 method of Grimme et al.[51]. During the structural relaxation, all atoms in the bottommost two layers were fixed to their bulk positions, whereas the remaining atoms together with the adsorbates were allowed to relax.

Previous theoretical studies[52,53] have shown that the binding energies are predominantly affected by the local bonding environment. Therefore, we focused on surface ensembles that exhibit different local bonding environments but with same alloying concentration. Specifically, we considered triatomic ensembles described in the form of Au_xIr_y where $x+y=3$, $x\geq 0$, $y\geq 0$, namely, Au_3, Au_2Ir_1, Au_1Ir_2, and Ir_3, as illustrated in Fig. 4c. These triatomic ensembles were modelled in four-layer 3 × 3 AuIr(111) slab models with the Au:Ir ratio fixed to 1:1. For each triatomic ensemble, we randomly generated ten different structures by maintaining the structure of the examined triatomic ensembles and varying the atoms around this structure. Then the adsorption energies of reaction intermediates in CO_2 reduction and the HER for these different structures were calculated, based on which the average values and corresponding error bars of adsorption energies can be determined. Similar to these triatomic ensembles, pure gold and iridium were also modelled by four-layer 3 × 3 Au(111) and Ir(111) slab models for comparison.

Data availability

Supporting data are available at the University of Michigan (https://doi.org/10.7302/w8ep-0g79). Further details regarding the data are available from the authors upon reasonable request.

References

1. De Luna, P. et al. What would it take for renewably powered electrosynthesis to displace petrochemical processes? *Science* **364**, eaav3506 (2019).
2. Zhang, B. & Sun, L. Artificial photosynthesis: opportunities and challenges of molecular catalysts. *Chem. Soc. Rev.* **48**, 2216–2264 (2019).
3. Pinaud, B. A. et al. Technical and economic feasibility of centralized facilities for solar hydrogen production via photocatalysis and photoelectrochemistry. *Energy Environ. Sci.* **6**, 1983–2002 (2013).
4. Lee, B.-H. et al. Electronic interaction between transition metal single-atoms and anatase TiO_2 boosts CO_2 photoreduction with H_2O. *Energy Environ. Sci.* **15**, 601–609 (2022).
5. Ali, S., Razzaq, A., Kim, H. & In, S.-I. Activity, selectivity, and stability of Earth-abundant CuO/Cu_2O/Cu^0-based photocatalysts toward CO_2 reduction. *Chem. Eng. J.* **429**, 131579 (2022).
6. Wang, L. et al. Surface strategies for catalytic CO_2 reduction: from two-dimensional materials to nanoclusters to single atoms. *Chem. Soc. Rev.* **48**, 5310–5349 (2019).
7. Habisreutinger, S. N., Schmidt-Mende, L. & Stolarczyk, J. K. Photocatalytic reduction of CO_2 on TiO_2 and other semiconductors. *Angew. Chem. Int. Ed.* **52**, 7372–7408 (2013).
8. Liu, W. et al. A scalable general synthetic approach toward ultrathin imine-linked two-dimensional covalent organic framework nanosheets for photocatalytic CO_2 reduction. *J. Am. Chem. Soc.* **141**, 17431–17440 (2019).
9. Wang, S. L. et al. Porous hypercrosslinked polymer–TiO_2–graphene composite photocatalysts for visible-light-driven CO_2 conversion. *Nat. Commun.* **10**, 10 (2019).
10. Reisner, E. et al. Molecularly engineered photocatalyst sheet for scalable solar formate production from carbon dioxide and water. *Nat. energy* **5**, 703–710 (2020).
11. Wang, Y. et al. Visible-light driven overall conversion of CO_2 and H_2O to CH_4 and O_2 on 3D-SiC@2D-MoS_2 heterostructure. *J. Am. Chem. Soc.* **140**, 14595–14598 (2018).
12. Iwase, A. et al. Water splitting and CO_2 reduction under visible light irradiation using Z-scheme systems consisting of metal sulfides, CoO_x-loaded $BiVO_4$, and a reduced graphene oxide electron mediator. *J. Am. Chem. Soc.* **138**, 10260–10264 (2016).
13. Andrei, V., Reuillard, B. & Reisner, E. Bias-free solar syngas production by integrating a molecular cobalt catalyst with perovskite-$BiVO_4$ tandems. *Nat. Mater.* **19**, 189–194 (2020).
14. Zhou, B. et al. Mo–Bi–Cd ternary metal chalcogenides: highly efficient photocatalyst for CO_2 reduction to formic acid under visible light. *ACS Sustain. Chem. Eng.* **6**, 5754–5759 (2018).
15. Kibria, M. G. et al. Atomic-scale origin of long-term stability and high performance of p-GaN nanowire arrays for photocatalytic overall pure water splitting. *Adv. Mater.* **28**, 8388–8397 (2016).
16. Li, X. et al. Selective visible-light-driven photocatalytic CO_2 reduction to CH_4 mediated by atomically thin $CuIn_5S_8$ layers. *Nat. Energy* **4**, 690–699 (2019).
17. Hao, L. et al. Surface-halogenation-induced atomic-site activation and local charge separation for superb CO_2 photoreduction. *Adv. Mater.* **31**, 1900546 (2019).
18. Cestellos-Blanco, S., Zhang, H., Kim, J. M., Shen, Y.-X. & Yang, P. Photosynthetic semiconductor biohybrids for solar-driven biocatalysis. *Nat. Catal.* **3**, 245–255 (2020).
19. Lin, S. et al. Covalent organic frameworks comprising cobalt porphyrins for catalytic CO_2 reduction in water. *Science* **349**, 1208–1213 (2015).
20. Chu, S. et al. Tunable syngas production from CO_2 and H_2O in an aqueous photoelectrochemical cell. *Angew. Chem. Int. Ed.* **55**, 14260–14264 (2016).
21. Chu, S. et al. Photoelectrochemical CO_2 reduction into syngas with the metal/oxide interface. *J. Am. Chem. Soc.* **140**, 7869–7877 (2018).
22. Hori, Y., Takahashi, I., Koga, O. & Hoshi, N. Selective formation of C_2 compounds from electrochemical reduction of CO_2 at a series of copper single crystal electrodes. *J. Phys. Chem. B* **106**, 15–17 (2002).
23. Wang, Y. et al. Catalyst synthesis under CO_2 electroreduction favours faceting and promotes renewable fuels electrosynthesis. *Nat. Catal.* **3**, 98–106 (2020).
24. Jeon, H. S., Kunze, S., Scholten, F. & Roldan Cuenya, B. Prism-shaped Cu nanocatalysts for electrochemical CO_2 reduction to ethylene. *ACS Catal.* **8**, 531–535 (2018).
25. Jung, H. et al. Electrochemical fragmentation of Cu_2O nanoparticles enhancing selective C–C coupling from CO_2 reduction reaction. *J. Am. Chem. Soc.* **141**, 4624–4633 (2019).
26. Kibria, M. et al. Visible light-driven efficient overall water splitting using p-type metal-nitride nanowire arrays. *Nat. Commun.* **6**, 1–8 (2015).
27. Li, Y. X., Sadaf, S. M. & Zhou, B. W. Ga(X)N/Si nanoarchitecture: an emerging semiconductor platform for sunlight-powered water splitting toward hydrogen. *Front. Energy* https://doi.org/10.1007/s11708-023-0881-9 (2023).
28. AlOtaibi, B., Fan, S. Z., Wang, D. F., Ye, J. H. & Mi, Z. T. Wafer-level artificial photosynthesis for CO_2 reduction into CH_4 and CO using GaN nanowires. *ACS Catal.* **5**, 5342–5348 (2015).
29. Kauffman, D. R., Alfonso, D., Matranga, C., Qian, H. & Jin, R. Experimental and computational investigation of Au_{25} clusters and CO_2: a unique interaction and enhanced electrocatalytic activity. *J. Am. Chem. Soc.* **134**, 10237–10243 (2012).
30. Back, S., Yeom, M. S. & Jung, Y. Active sites of Au and Ag nanoparticle catalysts for CO_2 electroreduction to CO. *ACS Catal.* **5**, 5089–5096 (2015).
31. Guan, X. et al. Making of an industry-friendly artificial photosynthesis device. *ACS Energy Lett.* **3**, 2230–2231 (2018).
32. Tran, P. D., Wong, L. H., Barber, J. & Loo, J. S. C. Recent advances in hybrid photocatalysts for solar fuel production. *Energy Environ. Sci.* **5**, 5902–5918 (2012).

33. Sreedhar, A. et al. Charge carrier generation and control on plasmonic Au clusters functionalized TiO_2 thin films for enhanced visible light water splitting activity. *Ceram. Int.* **44**, 18978–18986 (2018).
34. Wang, Y. X. et al. Deep ultraviolet light source from ultrathin GaN/AlN MQW structures with output power over 2 watt. *Adv. Opt. Mater.* **7**, 7 (2019).
35. Hafiz, S. et al. Determination of carrier diffusion length in GaN. *J. Appl. Phys.* **117**, 013106 (2015).
36. Zhou, B. et al. Gallium nitride nanowire as a linker of molybdenum sulfides and silicon for photoelectrocatalytic water splitting. *Nat. Commun.* **9**, 3856 (2018).
37. Zhou, B. et al. Highly efficient binary copper–iron catalyst for photoelectrochemical carbon dioxide reduction toward methane. *Proc. Natl Acad. Sci. USA* **117**, 1330–1338 (2020).
38. Chen, Y., Li, C. W. & Kanan, M. W. Aqueous CO_2 reduction at very low overpotential on oxide-derived Au nanoparticles. *J. Am. Chem. Soc.* **134**, 19969–19972 (2012).
39. Liu, M. et al. Enhanced electrocatalytic CO_2 reduction via field-induced reagent concentration. *Nature* **537**, 382–386 (2016).
40. Mistry, H. et al. Exceptional size-dependent activity enhancement in the electroreduction of CO_2 over Au nanoparticles. *J. Am. Chem. Soc.* **136**, 16473–16476 (2014).
41. Zhang, P., Wang, S., Guan, B. Y. & Lou, X. W. Fabrication of CdS hierarchical multi-cavity hollow particles for efficient visible light CO_2 reduction. *Energy Environ. Sci.* **12**, 164–168 (2019).
42. Vanka, S. et al. Long-term stability studies of a semiconductor photoelectrode in three-electrode configuration. *J. Mater. Chem. A* **7**, 27612–27619 (2019).
43. Kibria, M. G. et al. Atomic-scale origin of long-term stability and high performance of p-GaN nanowire arrays for photocatalytic overall water splitting. *Adv. Mater.* **2016**, 8388–8397 (2016).
44. Montoya, J. H., Shi, C., Chan, K. & Nørskov, J. K. Theoretical insights into a CO dimerization mechanism in CO_2 electroreduction. *J. Phys. Chem. Lett.* **6**, 2032–2037 (2015).
45. Zhou, Y. S. et al. Dopant-induced electron localization drives CO_2 reduction to C_2 hydrocarbons. *Nat. Chem.* **10**, 974–980 (2018).
46. Zhao, Y. et al. Direct C–C coupling of CO_2 and the methyl group from CH_4 activation through facile insertion of CO_2 into Zn–CH_3 σ-bond. *J. Am. Chem. Soc.* **138**, 10191–10198 (2016).
47. Perdew, J. P., Burke, K. & Ernzerhof, M. Generalized gradient approximation made simple. *Phys. Rev. Lett.* **77**, 3865–3868 (1996).
48. Kresse, G. & Hafner, J. Abinitio molecular-dynamics for liquid-metals. *Phys. Rev. B* **47**, 558–561 (1993).
49. Kresse, G. & Hafner, J. Ab-initio molecular-dynamics simulation of the liquid-metal amorphous-semiconductor transition in germanium. *Phys. Rev. B* **49**, 14251–14269 (1994).
50. Monkhorst, H. J. & Pack, J. D. Special points for Brillouin-zone integrations. *Phys. Rev. B* **13**, 5188–5192 (1976).
51. Grimme, S. et al. A consistent and accurate ab initio parametrization of density functional dispersion correction (DFT-D) for the 94 elements H–Pu. *J. Chem. Phys.* **132**, 154104 (2010).
52. Garcia, S. et al. Microwave synthesis of classically immiscible rhodium–silver and rhodium–gold alloy nanoparticles: highly active hydrogenation catalysts. *ACS Nano* **8**, 11512–11521 (2014).
53. Luo, L. et al. Tunability of the adsorbate binding on bimetallic alloy nanoparticles for the optimization of catalytic hydrogenation. *J. Am. Chem. Soc.* **139**, 5538–5546 (2017).

Acknowledgements

The work performed at the University of Michigan has been supported by the College of Engineering Blue Sky Research Initiative at the University of Michigan and United States Army Research Office Award W911NF2110337. B.Z. is grateful for financial support by the College of Engineering Blue Sky Research Initiative during his postdoctoral studies at the University of Michigan. J.S. and P.O. acknowledge financial support by the Natural Sciences and Engineering Research Council of Canada (NSERC) Discovery Grant (grant number NSERC RGPIN-2017-05187) and thank Compute Canada for providing computing resources. J.K.C. acknowledges support by the Liquid Sunlight Alliance (transient reflection spectroscopy), which is supported by the US Department of Energy, Office of Science, Office of Basic Energy Sciences, Fuels from Sunlight Hub under award number DE-SC0021266.

Author contributions

B.Z. and Z.M. conceived this project. B.Z., Z.Y., Y.M., P.W. and P.Z. conducted the co-catalyst deposition, APID characterizations, photocatalytic CO_2 reduction experiments and data analysis. P.O. conducted the DFT calculations with the assistance of X.-Y.L. and J.S. B.Z and Z.M. participated in discussion of the theoretical calculations. S.V. conducted the epitaxial growth of InGaN NWs with the assistance of Y.X. and I.A.N. T.M. performed the STEM characterization. H.S. collected the DRIFT spectra. J.K.C. carried out the transient reflection spectroscopy measurements and analysed these data. J.P. participated in analysis and discussion. B.Z., Z.Y., Y.M., P.O., J.S. and Z.M. wrote the paper with contributions from all the authors.

Competing interests

A US provisional patent has been filed based on this work by the inventors of Z.M., Z.Y., Y.M. and B.Z. Some intellectual property related to this work is licensed to NS Nanotech, Inc. and NX Fuels, Inc., which were co-founded by Z.M. The University of Michigan and Z.M. have a financial interest in these companies.

Additional information

Supplementary information The online version contains supplementary material available at https://doi.org/10.1038/s41929-023-01023-1.

Correspondence and requests for materials should be addressed to Baowen Zhou, Jun Song or Zetian Mi.

Peer review information *Nature Catalysis* thanks the anonymous reviewers for their contribution to the peer review of this work.